The Astrophysical Journal, 738:174 (10pp), 2011 September 10 doi:10.1088/0004-637X/738/2/174

THREE-DIMENSIONAL PHOTOIONIZATION STRUCTURE AND DISTANCES OF PLANETARY NEBULAE. IV. NGC 40

Hektor Monteiro[1] and Diego Falceta-Gonçalves[2]
[1] Departamento de Física, Universidade Federal de Itajubá, Av. BPS 1303-Pinheirinho, CEP 37500-903, Itajubá, Brazil; hektor.monteiro@gmail.com
[2] Escola de Artes, Ciências e Humanidades, Universidade de São Paulo, Rua Arlindo Bettio 1000, CEP 03828-000, São Paulo, Brazil; dfalceta@usp.br
Received 2011 March 4; accepted 2011 June 15; published 2011 August 24

ABSTRACT

Continuing our series of papers on the three-dimensional (3D) structure and accurate distances of planetary nebulae (PNe), we present here the results obtained for PN NGC 40. Using data from different sources and wavelengths, we construct 3D photoionization models and derive the physical quantities of the ionizing source and nebular gas. The procedure, discussed in detail in the previous papers, consists of the use of 3D photoionization codes constrained by observational data to derive the 3D nebular structure, physical and chemical characteristics, and ionizing star parameters of the objects by simultaneously fitting the integrated line intensities, the density map, the temperature map, and the observed morphologies in different emission lines. For this particular case we combined hydrodynamical simulations with the photoionization scheme in order to obtain self-consistent distributions of density and velocity of the nebular material. Combining the velocity field with the emission-line cubes we also obtained the synthetic position–velocity plots that are compared to the observations. Finally, using theoretical evolutionary tracks of intermediate- and low-mass stars, we derive the mass and age of the central star of NGC 40 as (0.567 ± 0.06) $M_{\odot}$ and (5810 ± 600) yr, respectively. The distance obtained from the fitting procedure was (1150 ± 120) pc.

Key words: methods: numerical – planetary nebulae: individual (NGC 40)

Online-only material: color figures

1. INTRODUCTION

Planetary nebulae (PNe) are end products of the evolution of stars with masses below 8 $M_{\odot}$ and as such have great importance in many fields in astrophysics, from basic atomic processes in solar-like stars to distant galaxies. Although the general picture of PNe formation is understood well (Kwok 2008), many questions remain unsolved such as the mechanism by which the stellar ejecta end up forming the many observed morphologies.

In the past, PNe have been studied with empirical methods and one-dimensional photoionization models. This scenario has recently been significantly changed with modern computational capabilities and software. As we have discussed in the previous papers of this series (Monteiro et al. 2004, 2005; Schwarz & Monteiro 2006), precise distances are of paramount importance to the study of these objects. To this extent our work provides precise, self-consistently determined distances for objects with comprehensive, in most cases spatially resolved, observational constraints. These objects can provide valuable calibration to pre-existing distance scales as well as self-consistently determined physical and chemical quantities.

One of the major limitations in our previous studies is related to the three dimensionality of both density structure and velocity field. In the previous papers of this series, even though we had well-determined density maps, the structures had to be defined by a combination of parametric surfaces such as spheres and ellipsoids with assumed density gradients to match the observations.

It is well known that hydrodynamical numerical simulations provide the nebular two-dimensional and/or three-dimensional (3D) density distributions and the velocity fields. Therefore, complex structures such as knots, clumps, or asymmetries arise naturally from physical processes. This is particularly important in asymmetric PNe, as the determination of physical parameters may be compromised by simplified toy models. Several numerical models have been proposed to explain the nebular morphologies, such as the two-wind interaction model (Icke et al. 1992), jets (Akashi & Soker 2008), magnetic fields (García-Segura et al. 2005), and even binarity, which accounts for anisotropic distribution of the asymptotic giant branch (AGB) wind or for the formation of bipolar jets.

Actual density distributions obtained from these simulations are, in general, directly compared to observed maps. However, it is well known that the gas density distribution—or even the column density projection along the line of sight (LOS)—may differ when compared to the observed maps. The difference may arise because the observations depend on the projected fluxes of certain spectral lines, which in turn depend on the 3D ionization structure. In this sense, only combined calculations of both hydrodynamics and photoionization processes can provide realistic emission maps.

In this work, we present a self-consistent model fit for NGC 40 using this new approach, employing both hydrodynamical and photoionization schemes. In the next section, we present the current knowledge about NGC 40 and the observational data used in our analysis. In Section 3, we present the numerical scheme and the hydrodynamical simulations for this object. The photoionization model is described and the results are shown in Section 4. Next, we discuss the kinematics of the nebular material combining the synthetic emissivities and the simulated data in Section 5, followed by a discussion and our conclusions.

2. NGC 40

NGC 40 is a well-studied object, classified as a low-excitation PN with a WC8-type central star (CS). Several imaging studies revealed a bright (slightly elliptical) core, a large halo, and filamentary structures (Chu et al. 1987; Balick 1987; Balick

et al. 1992; Meaburn et al. 1996). Clegg et al. (1983) presented optical and *IUE* spectra for the bright region of the nebula. Their results indicated that the abundances were typical and did not display large variations as expected for a WC8 CS. The authors argue that the CIV 1549 emission from the nebular envelope is too strong to have been produced by normal thermal processes, suggesting that it is a consequence of processes related to the wind of the CS.

Meaburn et al. (1996) obtained narrowband CCD images as well as long-slit echelle spectra and showed that the outer halo is moving with 31 km s^{-1}, with a turbulent motion of 7 km s^{-1}. The electron temperature for that region was calculated to be $T_e = (7400 \pm 160)$ K. The inner halo line profiles are split by about 50 km s^{-1}, which is consistent with the splitting seen in the bright core. The main outer clumps seen in narrowband images are shown to be kinematically associated with a barrel-shaped core, and thus are not the result of a true jet. The authors also find a dynamical age of ∼4000 yr from the expansion of the core. Koesterke et al. (1998) find the dynamical age 3500 ± 500 yr for NGC 40.

In Sabbadin et al. (2000) the authors present detailed tomography of NGC 40, obtained with echelle spectroscopy in many slit positions. By assuming a simple, direct position–velocity correlation they reconstruct the spatial distribution of H^+, O^{++}, and N^+. The results show a complex density structure with densities as high as 3000 cm^{-3}. The high densities found are in agreement with results obtained by (Leal-Ferreira et al. 2010, LGMR10 hereafter) who obtained values around 2500 cm^{-3}, although the errors are largely due to the weak lines used. The expansion velocities determined by Sabbadin et al. (2000) are around 25 km s^{-1}. The authors also point out that abundance gradients are likely to be present in the nebula, which is also consistent with the abundance maps of LGMR10, where the authors presented the first spatially resolved spectroscopic mapping of NGC 40.

In the infrared bands, Hony et al. (2001) reported the discovery of 21 μm and 30 μm emission features in the spectrum obtained from the *Infrared Space Observatory* (*ISO*). Based on the presence of the 21 μm feature, they argue that the bulk of the dust in the nebula has been produced during a carbon-rich phase before the atmospheres of these stars became hydrogen poor. The authors also present an estimation of the dynamical age of the object of ∼5000 yr. However, Cohen et al. (2002) ascribed the 21 μm feature to noise.

When considering the distance determinations, NGC 40 follows more or less the tendency of large interval that most PN determinations have. From the Acker catalog (Acker et al. 1994) we find $\langle d \rangle = 1019 \pm 357$ pc, ranging from 620 to 2070 pc.

2.1. Observational Data

The observational data used to constrain our model parameters in the present work were taken from different sources of the literature. We use spatially resolved emission-line maps as our main constraint in the ionization structure and spatial density and temperature distribution. The spatially resolved data comes from the work of LGMR10 described previously. We refer the reader to that work and references therein for greater detailed discussion.

For the absolute Hβ flux we use the value of Carrasco et al. (1983). The main reason is that the data obtained in LGMR10 were calibrated using only one star and the sky was not considered to be in photometric conditions. In this sense, the fluxes obtained from the LGMR10 data set are good for relative intensities only. We also use the integrated fluxes of (Liu et al. 2004, hereafter LLLB04) to help constrain the model integrated fluxes. Other works mentioned in the introduction were also used but with less weight in the final comparisons.

In the infrared band we used data values for NGC 40 obtained from the Two Micron All Sky Survey and the *IRAS* point source catalog, and also spectra from the *ISO* archives.[3] We also use fluxes at 9 and 18 μm obtained with the Infrared Camera and at 65, 90, 140, and 160 μm using the Far-Infrared Surveyor derived from the *AKARI* All-Sky Survey made available in Phillips & Marquez-Lugo (2011).

In order to model the kinematics of NGC 40 we used as constraints the line velocities obtained by Sabbadin et al. (2000), which obtained spatially resolved, long-slit echellograms of the nebula at *U*, *B*, and *V* filters and for different position angles. These data are used for the construction of synthetic tomographic maps of the nebula that are directly compared to the observations.

3. HYDRODYNAMICAL SIMULATIONS OF NGC 40

In order to obtain more realistic density and velocity distributions for the photoionization models, we performed a number of 2.5D hydrodynamical simulations of PN ejecta.

We have employed the grid code Godunov-MHD, which solves the gas hydrodynamical equations in conservative form. The effects of radiative cooling are calculated implicitly after each time step (see Falceta-Gonçalves et al. 2010a, 2010b, 2010c). The high-order shock-capturing scheme is based on an essentially non-oscillatory spatial reconstruction and Runge–Kutta time integration. The discontinuities that arise in simulations of supersonic expanding shells are better solved using the HLLC Riemann solver (Londrillo & Del Zanna 2000).

3.1. Setup for PN Ejection

As initial condition for this problem we use the basic model of two interacting winds (Icke et al. 1992), which represents the ejection of the tip-AGB stellar envelope over a preset density distribution given by the previous wind of the red giant star. To account for the giant-phase stellar wind density profile we set the ambient gas density as (Icke et al. 1989)

$$\rho_{\rm amb} = \frac{\rho_0}{A(\theta)} \left(\frac{r_0}{r}\right)^2, \quad (1)$$

where

$$A(\theta) = 1 - \alpha \left(\frac{e^{\beta \cos 2\theta - \beta} - 1}{e^{2\beta} - 1}\right). \quad (2)$$

The parameter α is related to the density ratio at the polar and equatorial directions, while β is the steepness of the density profile with the latitude. The initial temperature of the environment is defined as 100 K.

As mentioned previously, in the past two decades it has become clear that the two-wind interaction model is unable to reproduce the morphologies of most PNe. Many alternative models have been proposed including other dynamical mechanisms for the ejection and shaping of the PNe, such as jets (Sahai & Trauger 1998; Lee & Sahai 2003, 2004; Akashi & Soker 2008; Lee et al. 2009) and magnetic fields (García-Segura 1997; García-Segura et al. 1999). From a theoretical point of view, if

[3] *ISO* data tag: ADS/IRSA.Atlas#2010/1007/114440_6120

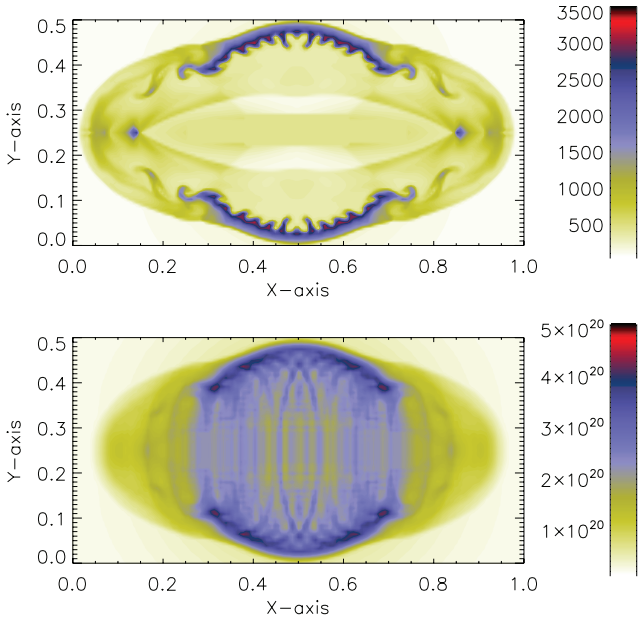

Figure 1. Density (top) and column density (bottom) maps for an inclination of 20° with respect to the plane of sky.

(A color version of this figure is available in the online journal.)

the magnetic pressure is of the order of the kinetic and thermal energy densities we should expect a larger degree of collimation of the lobes. A similar effect would be expected in a heavy jet scenario. In a situation with any of these two mechanisms the resulting α and β parameters would be slightly different. In this work, however, we decided to use the simpler two-wind interaction model in order to reduce the number of free parameters in modeling the dynamical properties of this specific object.

We performed 2.5D simulations for different sets of α and β parameters in order to obtain the most similar projected density distribution to the observed morphology for NGC 40. We run models varying α from 0.0 to 0.9, in steps of 0.1, and β from 0.0 to 6.0, in steps of 0.5. Due to computational limitations it was impossible to run the models in three dimensions. All models were calculated with a fixed grid of 512×256 resolution. The cell size is defined as 2.2×10^{15} cm and the simulation box is 1.15×10^{18} cm wide. The simulations were run up to a dynamical time of 10,000 yr. The structure adopted for the nebulae is constrained by the observed density map and the observed projected morphology. The best model for this particular object was obtained for $\alpha = 0.3$ and $\beta = 5.0$, as described below.

3.2. Hydrodynamical Results

The initial distribution of density is determined by the anisotropic wind from the AGB star. At the center of the cube, the ejection of the second and faster wind compresses the environment gas, resulting in the nebular structure. The initial anisotropy of the pre-nebular wind and of the post-ejection wind results in a roundish structure with two lobes. In Figure 1 (top), we show the density distribution obtained at $t = 5900$ yr. At this time the size of the structure is ~61,500 AU wide. The nebular peak density is ~2800 cm^{-3} at the roundish structure. Here, the visible filaments are formed by a Rayleigh–Taylor (RT) instability that arises as the lighter and warmer plasma expands onto the cold and dense structure.

At both opposing sides along the major axis of the nebula, the round structure is opened forming two lobes. As the internal wind material propagates outward it reaches the inner shock. Since the expanding gas is not isotropic, the streamlines cross the shock surface obliquely, resulting in a deviation of the flow. The material flowing along the nebular shell then converges at the apex of the lobe, in the so-called shock-focused inertial confinement, resulting in a dense structure, as seen in Figure 1, and eventually in a jet (Frank et al. 1996). At the stage of the nebula in this simulation there is no jet formed. The lobes present numerical densities of ~1000 cm^{-3}, except for the two opposing knots—also formed by RT instability—at the edges of the major axis of the structure, which are 50% denser. The ejecta average velocity is ~25 km s^{-1}.

Besides the main nebula seen with densities >1000 cm^{-3}, a diffuse gas with densities ~500 cm^{-3} surrounds the whole structure. The inner surface is determined by the reverse shock of the main nebula with the expanding hot wind of the central source. The white dwarf wind blows the hot and low-density (<200 cm^{-3}) gas which is, in general, observed in X-rays.

Despite the fact that the simulation is performed in 2.5D, the structure may be considered of cylindrical symmetry. Therefore, it is possible to rotate the physical variables around the nebular major axis of symmetry in order to obtain a 3D distribution. We must point out here that when this approximation is used the small-scale structures, such as those generated by the RT instabilities mentioned above, will appear in the column density maps as circles/rings instead of knots, as would be expected from 3D simulations. For the purposes of the present work this limitation does not influence our results. With the cube of density it is possible to integrate it and obtain the column density for several lines of sight. In Figure 1 (bottom), we illustrate the projected column density for an inclination angle of 20° for the major axis with respect to the LOS. The column density map shows similar features as seen in the density map, except for the missing two opposing knots located at the end of the major axis of the nebula. The reason for that is the small size of these clumps. Interestingly, two opposing knots at the major axis are visible in the observed maps of NGC 40. As we show further in this paper, the synthetic maps obtained after computing the photoionization reveal the existence of the knots for low-ionization lines, such as S II and N II.

4. PHOTOIONIZATION MODELS FOR NGC 40

In the present work, we used the photoionization code Mocassin 3D (version 2.02.54) described in full detail in Ercolano et al. (2003).

The procedure for studying NGC 40 is the same adopted in previous papers of this series, i.e., we provide a density distribution of the nebular plasma and run a Monte Carlo simulation using the Mocassin 3D code for the radiative transfer, assuming a given luminosity (L_ν) from the central source. The whole process is iterated until reasonable agreement with observational constraints is achieved. The main improvement of this work with respect to the previous ones is the use of a self-consistent distribution of density from the numerical hydrodynamical simulations. In the following subsections we discuss the input parameters used.

4.1. The Ionizing Source

The choice of the ionizing source in photoionization models is far from being the trivial choice of a blackbody curve of a given temperature. Recent developments in the modeling of stellar atmospheres have provided more complex stellar spectra

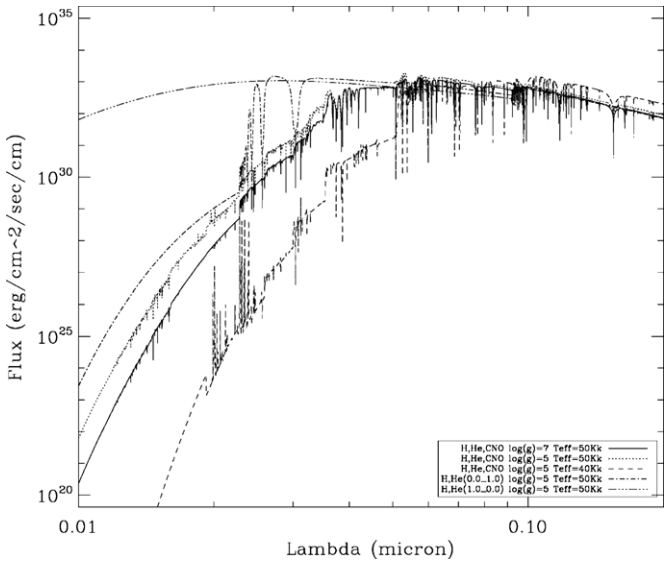

Figure 2. Central star ionizing spectra studied in this work.

that can be used with physical and chemical parameters, such as log(g) and abundances of the elements which may be important.

In the field of PNe CS the standard choice of models is the grid provided by T. Rauch[4] where the user can find NLTE stellar model atmosphere fluxes which cover the parameter range of PN ionizing sources: $T_{\rm eff} = 50$–190 kK, log(g) = 5–9 (cm s^{-2}), and distinct abundances.

We have explored a set of CS models to obtain a best match to the observed PN line intensities in NGC 40. The different spectra used are shown in Figure 2. The photoionization code was run with the density distribution obtained from the hydrodynamical simulation, as shown in Figure 1 (transformed in 3D). The plots differ from log(g), $T_{\rm eff}$, and chemical abundances, which are described in Table 1. We found best-fitting models for each CS star studied giving more emphasis on reproducing the total Hβ flux first and then other emission lines. The final step consisted of fine tuning the abundances of elements that are more sensitive to the $T_{\rm eff}$ such as oxygen, in an attempt to reproduce the observed line fluxes.

As expected, the spectra seem very similar at the region that contributes most for the ionization of H, making it hard to select an ionizing source based only on the total Hβ flux. To pinpoint the best spectrum we must analyze other emission lines produced at different regions of the nebula and by ions sensitive to the ionizing source temperature. We point out that the He II 4686 emission line is one of the best to constrain $T_{\rm eff}$; however, it is too weak in NGC 40 and could not be used. The most relevant differences appear in the oxygen lines as can be seen in Table 1, where the last column shows the observed values obtained from LLLB04 and LGMR10.

From the data presented in Table 1 we infer that the best ionizing spectrum was the one with [H:He:CNO] 0:0.33:0.67, which are typical values for a PG 1159 type star (hydrogen-deficient post-asymptotic giant branch stars believed to be descendents of WC-type stars). For a very detailed review of PG 1159 stars see Werner & Herwig (2006). Obviously, due to computational limitations, the grid search for the ionizing source was not exhaustive. However, we explored the most likely alternatives given the current knowledge of PN ionizing sources and observation data for NGC 40.

4.2. Dust

Apart from the main emission lines, NGC 40 also presents large continuum fluxes that are related to the dust component, as observed in infrared bands. Therefore, we have also included

[4] Available at http://astro.uni-tuebingen.de/~rauch/

Table 1
Observed and Model Line Fluxes and Model Central Star Parameters for NGC 40

Characteristic	CS1	CS2	CS3	CS4	CS5	CS6	Observed[a]
H:He:CNO	1:0:0	0:1:0	0:1:0	0:0.33:0.67	0:0.33:0.67	0:0.33:0.67	
Teff	50 kK	50 kK	50 kK	40 kK	50 kK	50 kK	
log(g)	5	5	7	5	5	7	
Hβ flux[b]	0.032	0.034	0.031	0.033	0.037	0.036	0.038
He II4686	0.157	0.000	0.000	0.000	0.000	0.000	0.000
[N II]5755	0.051	0.041	0.064	0.03	0.04	0.05	0.03
[N II]6548	0.774	0.705	0.852	0.98	0.84	0.90	0.85
[N II]6584	2.365	2.154	2.602	2.99	2.56	2.75	2.54
[O II]3726	0.078	0.066	0.240	1.110	0.881	2.381	2.571[c]
[O II]3729	0.052	0.043	0.149	0.717	0.534	1.442	1.904[c]
[O III]4363	0.006	0.005	0.007	0.000	0.004	0.004	0.005
[O III]4959	0.193	0.170	0.189	0.000	0.172	0.196	0.193
[O III]5008	0.576	0.509	0.563	0.000	0.514	0.585	0.589
Line Diagnostics							
Ne:							
[S II]6731/6717	1.166	1.206	1.242	1.236	1.275	1.261	1.308
[O II]3729/3726	0.667	0.650	0.621	0.640	0.606	0.605	0.739
Te:							
[N II](6584+6548)/5755	61.826	69.695	54.138	132.8	82.9	80.7	74.4
[O II]3726/7320	19.005	20.575	16.052	33.8	21.7	21.3	36.7
[O III](4959+5007)/4363	126.95	152.190	103.041	···	171.6	195.3	156.4

Notes.
[a] Relative fluxes from Leal-Ferreira et al. (2010).
[b] 1×10^{36} erg cm^{-2} s^{-1}.
[c] Relative fluxes from Liu et al. (2004).

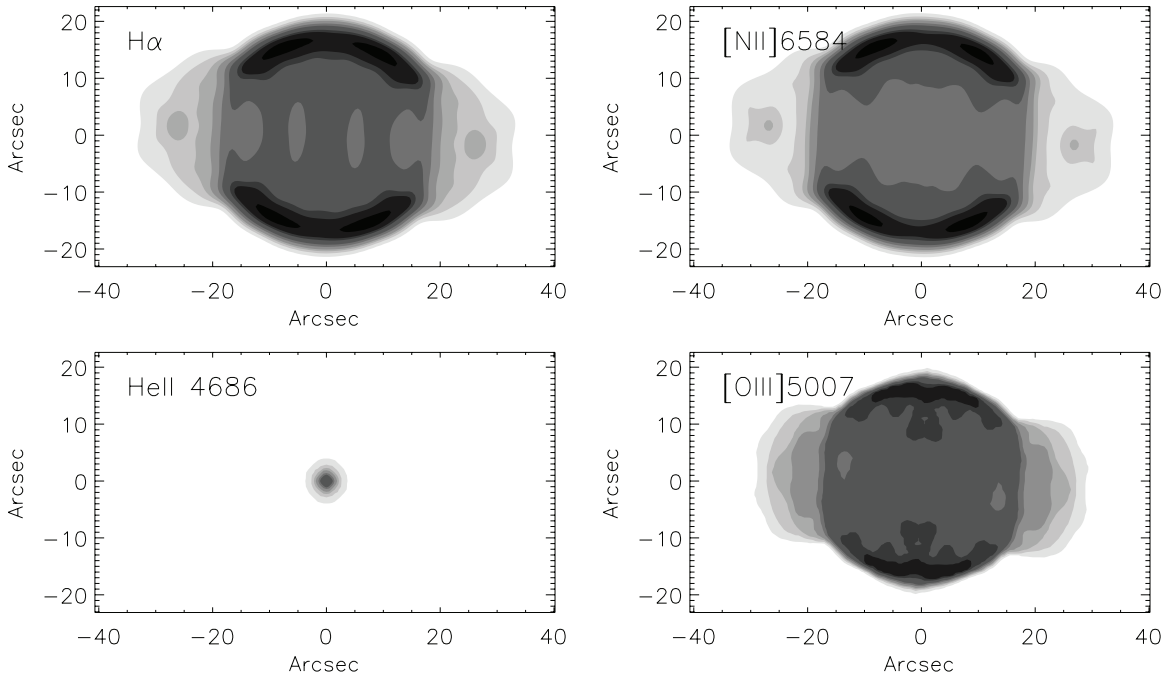

Figure 3. Synthetic images obtained from the projection of the data cubes of emissivities calculated by the photoionization code for four of the most important emission lines. The nebula has been rotated with an angle of 20° with respect to the plane of sky.

dust in the modeling, taking advantage of the full potential of the Mocassin 3D code. As discussed above, some authors have already dealt with the infrared data and dust content of this object. The main goal in the present work is to establish reasonable intervals for the amount of dust present as well as some information on its properties, rather than obtaining an excellent fit for the infrared observations.

To constrain the model dust parameters we have gathered the spectra obtained by *ISO* as well as photometry in the *IRAS* catalog. The *ISO* spectra was obtained from the NASA/IPAC Infrared Science Archive. We also use fluxes at 9, 18, 65, 90, 140, and 160 μm using the data made available in Phillips & Marquez-Lugo (2011).

The input parameters for the dust obtained from the fitting procedure were, assuming the dust to be perfectly mixed with the gas, a mass dust-to-gas ratio of 0.0015 with a typical Mathis–Rumpl–Nordsieck dust model (MRN; Mathis et al. 1977) size distribution and composition of 50% silicates, 40% grafites, and 10% polycyclic aromatic hydrocarbon grains. The data tables for the dust parameters are those available in the Mocassin dust data directory and we refer the reader to Ercolano et al. (2005) for details.

5. PHOTOIONIZATION MODEL RESULTS

In this section we present the main results from the final fitted model for NGC 40.

5.1. Synthetic Observational Maps of NGC 40

Once the emissivity at each wavelength is obtained, from the best-fit photoionization model, it is possible to construct the synthetic observational maps of NGC 40. In order to accomplish this we integrated the emissivity cube along a given LOS. In Figure 3, we show the synthetic maps obtained for the Hα, [N II]6584, He II, and [O III]5007 spectral lines assuming an inclination of 20° for the nebular major axis with respect to the plane of sky.

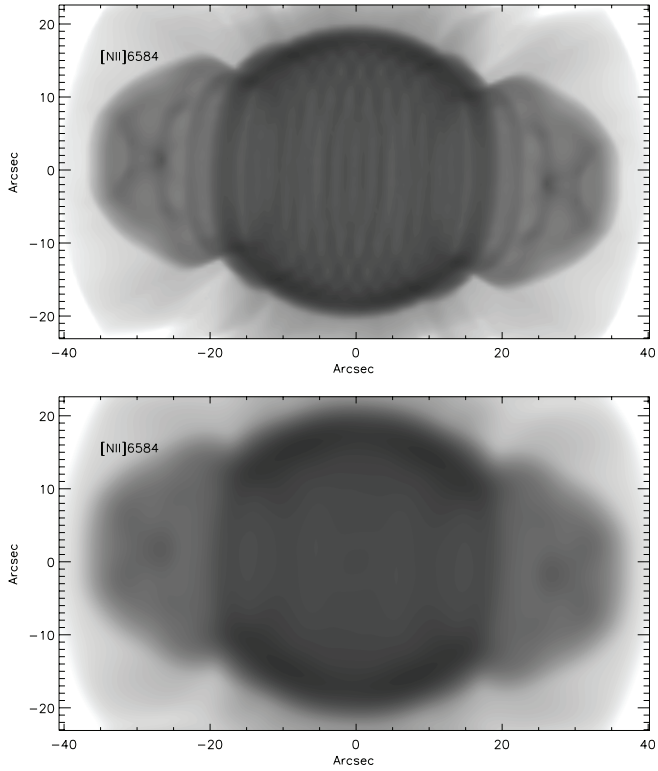

Figure 4. Model [N II]6584 images obtained from the best-fit model. The upper image shows the raw model cube projected with orientation as described in the text and lower image shows the same projection but convolved with a 3″ PSF to match the resolution of LGMR10 maps.

These synthetic maps cannot be directly compared to the observations due to the different spatial field resolution. The numerical simulations presented here present finer resolution when compared to the observed maps of LGMR10. In this sense, in order to match their spatial resolution we convolved the synthetic maps with a 3″ point-spread function (PSF). In

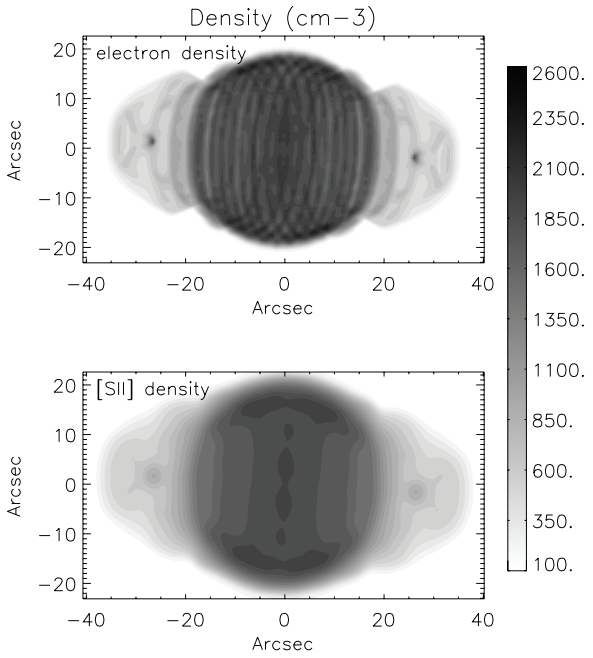

Figure 5. Electron density maps obtained from the photoionization model. The upper panel shows the projected electron density cube, weighted by the [S II]6717 emissivity cube. The lower panel shows electron density obtained from the usual diagnostic ratio using the convolved emission-line maps.

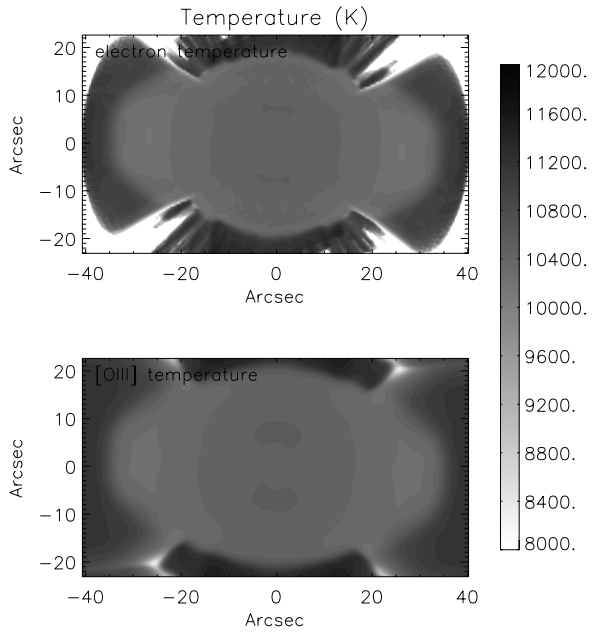

Figure 6. Electron temperature maps obtained from the photoionization model. The upper panel shows the projected electron temperature cube, weighted by the [O III]4363 emissivity cube. The lower panel shows electron temperature obtained from the usual diagnostic ratio using the convolved emission-line maps.

Figure 4, we show the original synthetic map for the emission line [N II]6584 (top) and the convolved map for the same line (bottom). Despite the coarser spatial resolution, the knots seen at the ends of the major axis of symmetry are still visible and the general morphology of the nebula is kept. At smaller scales, the inhomogeneities created by the RT instabilities are smoothed.

In Figure 5, we present two density maps obtained from the model. The first map in the upper panel was obtained from the projection of the electron density data cube weighted by the [S II]6717 emissivity cube. The lower panel shows the density map obtained from the usual ratio of the convolved [S II] emission-line maps. The two show good agreement despite the different methods used in the calculation.

In Figure 6, we present two electron temperature maps obtained from the model. The first map in the upper panel was obtained from the projection of the electron temperature data cube weighted by the [O III]4363 emissivity cube. The lower panel shows the electron temperature map obtained from the usual diagnostic ratio [O III]5007 + 4959/[O III]4363, again using the convolved emission-line maps. Again, apart from the difference in resolution we see good agreement in the values obtained.

In Figure 7, we present the observed Hα narrowband emission map superimposed by the contours of the convolved synthetic map from the best-fit model (taking into account the ∼15% [N II] contamination in the narrowband filter). The agreement between both, the size and morphology of the true nebular emission, and the presented model is clear.

The total line intensities of the best-fit model are given in Table 2, as well as the fitted abundances and ionizing source parameters. To estimate a final relative uncertainty to be used in the fitted model parameters we calculated the relative errors for all lines in Table 2, using the average of the observed values when both LLLB04 and LGMR10 are present. The final relative uncertainty can be obtained by taking a weighted average of all relative errors, using line intensities as the weights. The value

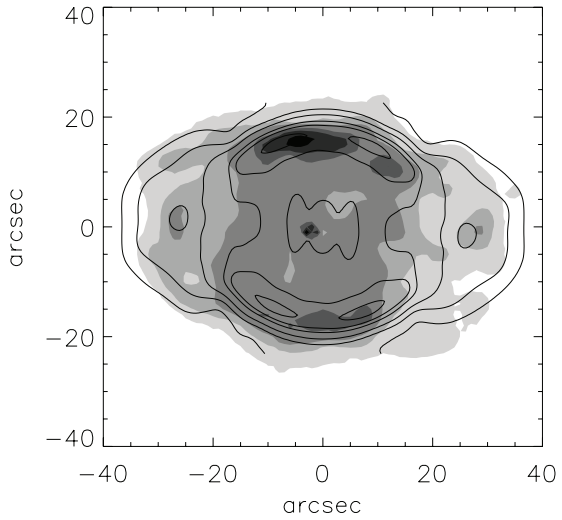

Figure 7. Image comparing the observed Hα narrowband image with the contours of the equivalent image from the fitted model.

obtained is 10%, which we adopt as the best estimate of the relative 1σ uncertainty of our final fitted parameters.

The model fitting procedure which uses, among other constraints, the model image size fitted to the observed one for Hα, as well as the absolute Hβ flux, gives a final distance of 1150 ± 120 pc for NGC 40.

In Figure 8, we present the total spectral energy distribution (SED) obtained from the best-fit model (solid line), compared to the *ISO* spectra (gray dashed line), *UBVRI–JHK* (for the central source only), and *IRAS* photometric data (circles). Here, as mentioned above, we assumed the dust to be perfectly mixed with the gas and adopted a mass dust-to-gas ratio of 0.0015, with a typical MRN size distribution and composition. The dust-to-gas mass ratio is in good agreement with the 0.0013 value obtained by Stasińska & Szczerba (1999).

Table 2
Observed and Model Line Fluxes and Model Central Star Parameters for NGC 40

Characteristic	LLLB04	LGMR10	ModPG
T_* (kK)			50
$L_*/L_\odot$			1736
log(g)			7
Density (cm^{-3})	1750	100–2700	100–2600
He/H	1.2×10^{-1}	1.2×10^{-1}	0.9×10^{-1}
C/H	6.9×10^{-4}	–	6.5×10^{-4}
N/H	8.5×10^{-5}	–	6.8×10^{-5}
O/H	4.9×10^{-4}	4.1×10^{-5}	1.9×10^{-4}
S/H	2.6×10^{-6}	–	6.8×10^{-6}
Cl/H	8.1×10^{-8}	–	7.3×10^{-8}
log(Hβ)	−9.62	–	−9.61
[O II] 3726	2.57	...	2.61
[O II] 3728	1.90	...	1.52
H10 3797	0.05	0.04	0.05
H9 3835	0.08	0.07	0.07
H8+He I 3888	0.18	0.17	0.22
Hδ 4101	0.28	0.22	0.26
Hγ 4340	0.50	0.44	0.47
[O III] 4363	0.003	0.006	0.004
He I 4471	0.03	0.02	0.05
He II 4686	0.00	0.01	0.00
He I 4921	0.01	0.01	0.01
[O III] 4959	0.14	0.19	0.19
[O III] 5007	–	0.59	0.57
[N I] 5198	0.01	0.00	0.00
[Cl III] 5517	0.004	0.004	0.005
[Cl III] 5537	0.004	0.005	0.005
[O I] 5577	–	0.006	0.00
[N II] 5755	0.03	0.03	0.04
He I 5876	0.09	0.11	0.13
[O I] 6300	0.03	0.03	0.02
[O I] 6363	0.01	0.01	0.01
[N II] 6548	0.87	0.85	0.83
Hα 6563	2.99	2.97	2.85
[N II] 6584	2.67	2.54	2.94
He I 6678	0.03	0.02	0.03
[S II] 6717	0.12	0.13	0.14
[S II] 6731	0.16	0.19	0.18
[C IV] 1550	0.26	...	0.00
C II 2841	0.04	...	0.007
[C II] 158 μm	0.038	...	0.036

6. POSITION–VELOCITY DIAGRAM

One of the advantages of combining hydrodynamical simulations with photionization calculation is the possibility of obtaining self-consistent PV diagrams. The synthetic PV diagrams for NGC 40 can be directly compared to those obtained observationally by Sabbadin et al. (2000).

From the hydrodynamical simulations we obtained the velocity field (**u**) and from the photoionization code Mocassin 3D we obtained the emissivity for the main nebular spectral lines (ϵ^λ). The line profiles (I_v) are obtained as (Falceta-Gonçalves et al. 2006)

$$I_v = \sum_{i=1}^{i_{\max}} \frac{\epsilon_i^\lambda}{(2\pi\sigma^2)^{1/2}} \exp\left[-\frac{\left(v - u_{\rm LOS}^i\right)^2}{2\sigma^2}\right], \qquad (3)$$

where the indices i represent each cell of the cube intercepted by the LOS, $u_{\rm LOS}$ is the projected velocity along the LOS, ϵ_i^λ is the emission of a given line λ at the ith cell, and σ is the thermal Doppler broadening.

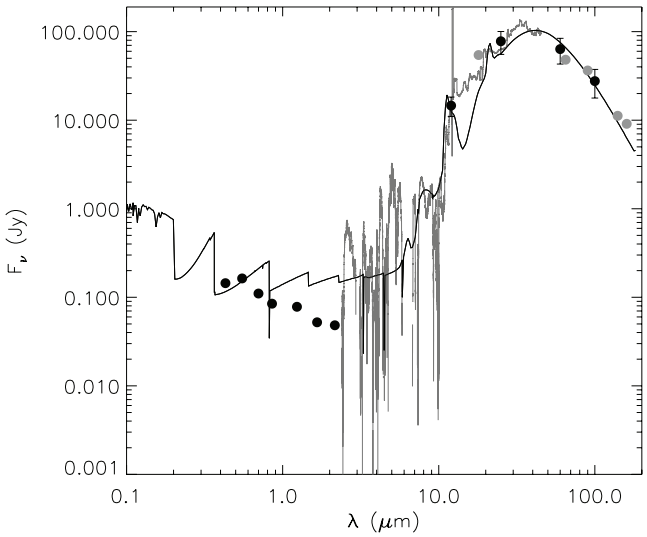

Figure 8. Model SED (solid line) for NGC 40 compared to *ISO* spectra (gray dashed line) and *UBVRI*, *JHK* (both for central source only), and *IRAS* photometric data obtained from SIMBAD.

The result of Equation (3) is a 3D variable $P \times P \times V$ that may be converted into a standard PV diagram once a specific direction (the position angle) is chosen, representing the observational long slit. Detailed observed PV diagrams for NGC 40 were presented by Sabbadin et al. (2000). In this section, we compare their data with the synthetic line profiles obtained from the simulations. Both observational (red circles) and synthetic (gray-scale) data for [N II] 6584 are shown in Figure 9. The synthetic spectral line profiles were obtained for different inclination angles with respect to the LOS, ranging from $\theta = 0^\circ$ (left) to 40° (right), and for two position angles for the slit: top—along the minor axis of symmetry—and bottom—along the major axis of symmetry of the nebula. Visually it is possible to estimate a best match for $\theta \sim 20^\circ$.

In Figure 10, we present the synthetic PV diagrams obtained from the emission maps of H, [N II], [S II], and [O III], respectively. The circles represent the observed data for [N II] 6584, for comparison. The plots obtained for H, [N II], and [S II] are very similar. The knots are visible as the darker spots at the edges of the position angle (P.A. $\sim \pm 30^\circ$), with an expanding velocity $|v| \sim 10$ km s^{-1}. These clumps are not detected in the [O III] maps, confirming their low ionization. On the other hand, the [O III] PV diagram obtained along the minor axis of symmetry (top) shows emission at positions closer to the central source compared to H, [N II], and [S II]. These general results corroborate with the observations of Sabbadin et al. (2000) and show that both the density distribution and the velocity field obtained from the simulations agree with the observational data of NGC 40.

7. DISCUSSION AND CONCLUSIONS

We have obtained a self-consistent 3D model for PN NGC 40. Unlike previous studies we have defined the 3D density structure by using a 2.5D hydrodynamic simulation as described in Section 3. With the model density structure we then proceeded to the usual 3D photoionization modeling procedure performed and described in detail in previous papers of this series.

Though the hydrodynamical simulations do include the effects of radiative cooling, we do not treat the effects of

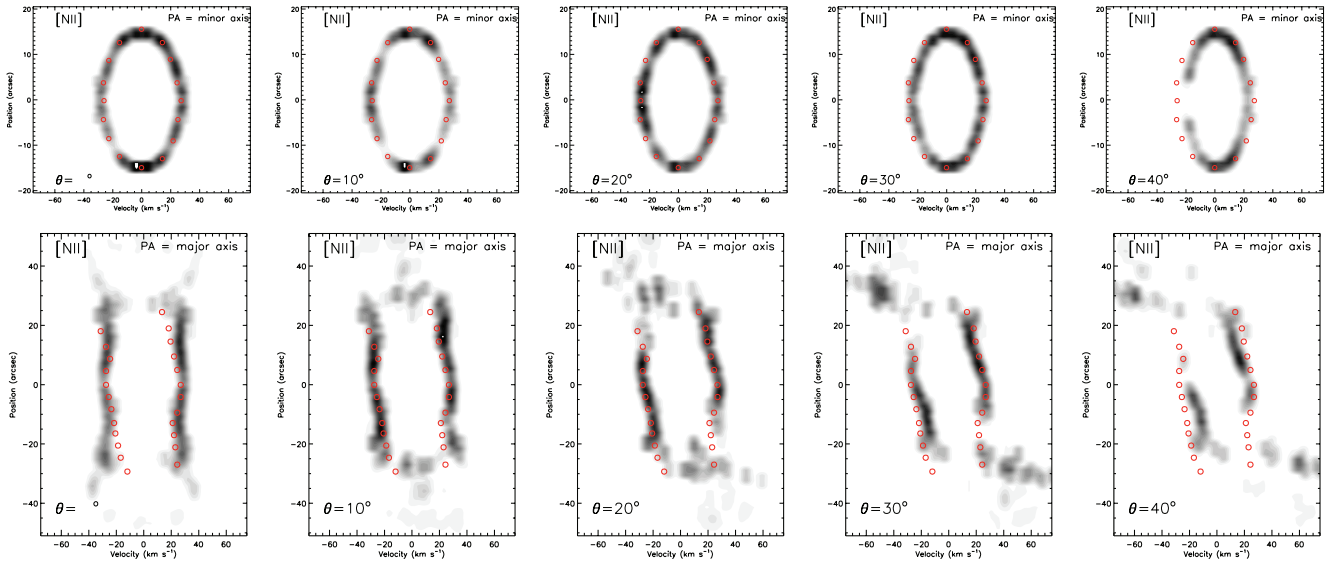

Figure 9. Position–velocity diagrams obtained from the emission maps of [N II] combined with the velocity cubes from the hydrodynamical simulation, for different inclination angles of the PN axis of symmetry, and the LOS (0°, 10°, 20°, 30°, and 40°). The top row represents the P.A. along the minor axis of the PN projected at the plane of the sky, while the bottom row is for the major axis. Circles represent observed values extracted from Figures 3 and 4 of Sabbadin et al. (2000).

(A color version of this figure is available in the online journal.)

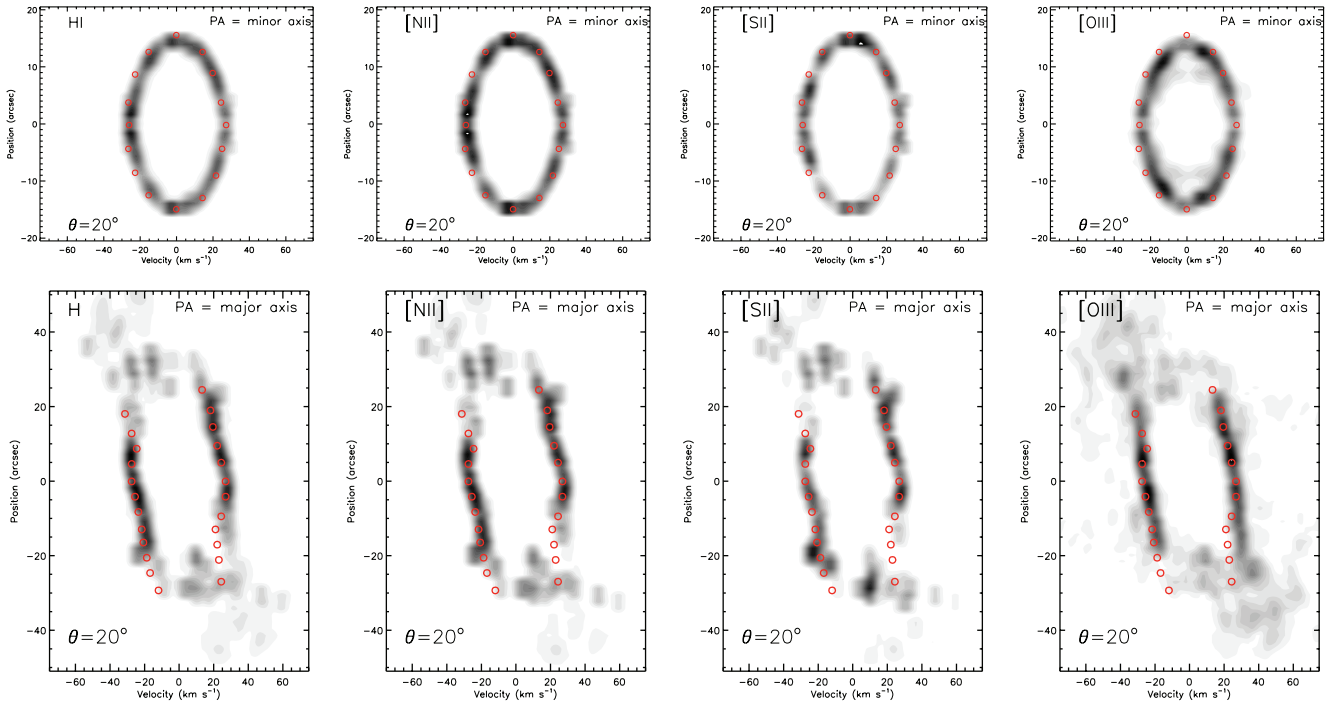

Figure 10. Position–velocity diagrams obtained from the emission maps of H, [N II], [S II], and [O III] combined with the velocity cubes from the hydrodynamical simulation for an inclination angle of 20°. The top row represents the P.A. along the minor axis of the PN projected at the plane of the sky, while the bottom row is for the major axis. Circles represent observed values for [N II] extracted from Figures 3 and 4 of Sabbadin et al. (2000).

(A color version of this figure is available in the online journal.)

heating and ionization from the central source. However, ionization fronts are known to significantly change the propagation of shock fronts under certain conditions (see Henney et al. 2005 for review). From Henney et al. (2005), the role of photoionization advection is related to the advection parameter

$$\lambda_{\rm ad} = \frac{\xi_{\rm ad} M}{\tau - \xi_{\rm ad} M},$$

defined as the ratio between the fluxes of atoms and photons at the ionization front, with M being the mach number, $\xi \sim 12$ for typical CS parameters and sound speed at the ionization front, and $\tau \sim 10^{-18} nz$, with z being the characteristic Stromgren distance. For NGC40, at the evolutionary stage analyzed in this work, $z \sim 10^{17}$–10^{18} and $n \sim 3000$, we obtain $\tau \sim 300$–3000, which leads to $\lambda_{\rm ad} \sim 0.004$–$0.04\,M$, i.e., the thickness of the ionization front is very small. In such a situation the effects of the ionization front in the dynamical evolution of the nebula are negligible, and the instabilities are, in general, quenched (Williams 2002).

The density and projected column densities obtained from the numerical simulations agree with the observed large-scale morphology of NGC 40. The column density projections,

however, do not show the knots at the major axis of symmetry of the nebula as observed at low-ionization energy lines, such as [N II]6584. After using the simulated nebula as inputs for the photoionization code Mocassin 3D, the resulting emissivities in this line showed good agreement with the observed maps also in smaller morphological scales such as the knots. This reveals the importance of combining both hydrodynamical and photoionization models in order to study the true nature of the nebular plasma.

Martin et al. (2002) reported the detection of emission-line structures due to the interaction of the PN with the interstellar medium attributed to RT instability. Indeed, this is observed in the simulations.

In the X-rays band, NGC 40 presents a faint and diffuse emission distributed within a partial annulus of about 40″ in diameter (Montez et al. 2005). The morphology, temperature, and luminosity inferred from these observations indicate that the emission arises from a hot bubble generated by shocked quasi-spherical fast wind from the CS. The results also show no evidence for collimated jets. In the simulations, as shown in Figure 1, the reverse shock interacts with the continuous wind from the central source creating a low-density and high-temperature medium. This region may be associated with the observations in X-rays.

The results show good agreement with all observables chosen as constraints to the modeling. The usual diagnostic maps (density and temperature) as well as all emission-line maps obtained by LGMR10 are nicely reproduced. We also reproduce with a good degree of agreement the kinematical data obtained by Sabbadin et al. (2000).

The total line fluxes as well as the total Hβ flux are reproduced within the observational uncertainties for a fitted distance of 1150 ± 120. The uncertainty in the distance was estimated based on the relative errors of observed total line fluxes relative to model values and estimated errors of observed and model emission-line map characteristics done by visual comparison. This result is in good agreement with the average result and uncertainty obtained from many different literature values. The good agreement of the size obtained with our structure and distance value is clearly seen in Figure 5, where we overlay the model contours of a simulated Hα + 15%[N II] image with the respective observed one from an Hα narrowband filter.

In Figure 11, we compare the values of effective temperature and luminosity obtained from our model, $T_{\rm eff} = (50 \pm 5)$ kK and $L = (1719 \pm 170)\ L_{\odot}$, to evolutionary tracks of Vassiliadis & Wood (1994) and estimate an age of (5810 ± 600) yr, for a core mass of $(0.567 \pm 0.06)\ M_{\odot}$ formed from a progenitor with $(1 \pm 0.1)\ M_{\odot}$. The age value is in good agreement with literature values mentioned in Section 1.

The characteristics of the ionizing source and position in the $T_{\rm eff} \times L$ diagram, as shown in Figure 9, are consistent with a WC star in transition to a PG1159 type object. This evolutive connection with sequence [WCL] → [WCE] → ([WC]+PG1159) → PG1159 was proposed by Koesterke et al. (1998). It is interesting to note the discrepancy between our model results and previous ones from empirical methods from the literature. These discrepancies are also present in most other objects studied using our method. The lower number of assumptions and simplifications, as well as the large amount of observational constraints, used in our work indicates that the values obtained are likely more accurate.

Morisset & Georgiev (2009) argue that the method of determining distances with self-consistent modeling could be wrong

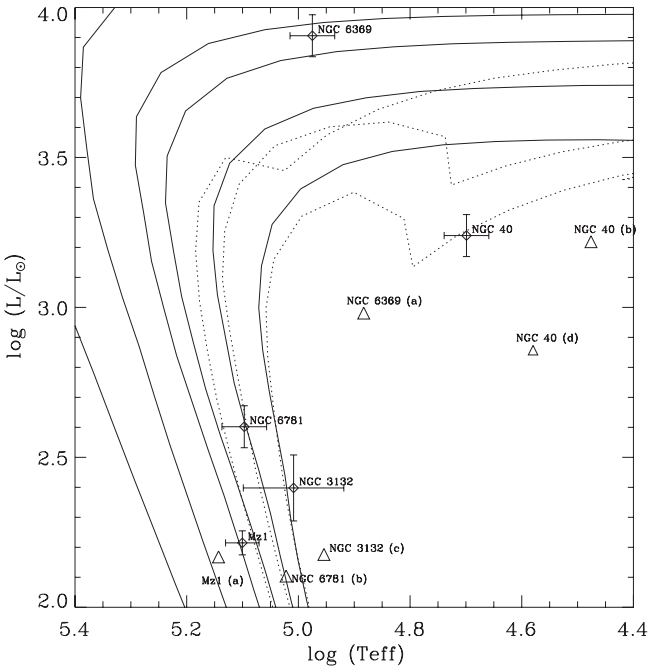

Figure 11. H-R diagram for NGC 6781, NGC 3132 (Monteiro et al. 2000), NGC 6369 (Monteiro et al. 2004), and MZ 1 (Monteiro et al. 2005)—all PNe that had their central star properties determined by our method. Also plotted are the literature values for comparison. (a) Stanghellini et al. (1993), (b) Stanghellini et al. (2002), (c)Baessgen et al. (1990), and (d) Pottasch & Bernard-Salas (2010). The evolutionary tracks are from Vassiliadis & Wood (1994); they are similar to the Blöcker (1995) models but take metallicities into account.

if the existence of a clumping factor is assumed. While this is theoretically true, the use of clumping factors are not justified in the methods developed in our work where the 3D structure used is defined down to the cube cell resolution scale. This is especially true in the present work since the fluctuations that appear in the density structure we have obtained are solely due to hydrodynamical processes and no artificial factor is needed.

In any case, we follow the exercise suggested by Morisset & Georgiev (2009) in their Section 5.4 to determine the clumping factor. We have obtained a relation from the Vassiliadis & Wood (1994) model tracks in the temperature range of the effective temperature obtained by our models for NGC 40. The relation we obtained was $\log(\text{age}) = 12.025 - 2.543 \log(L/L_{\odot})$. It is important to point out that it is not clear from Morisset & Georgiev (2009) exactly how their relation was obtained. We selected points from the evolutionary tracks of the He-burning models in a temperature range of $4.6 < \log(T_{\rm eff}) < 4.8$ and fitted a straight line to the region close to the luminosity range needed.

Using the luminosity and dynamical age obtained from our model fits we find the intersection to the relation above and obtain a value of $k1$. Given that this method is very crude and indirect and errors are difficult to estimate it is impossible to obtain a reliable confidence interval. If we use the lowest literature value for the dynamical age, 3500 years (Koesterke et al. 1998), we obtain $k1.2$. Given that the relative error quoted for the age is about 15%, we consider this to be consistent with a clumping factor of 1, within the errors.

In line with all the observational constraints used, although very crude and indirect, the calculations above give some independent evidence that there is no need for the artificial clumping factor, also indicating that the distance determined for NGC 40 is reliable.

Table 3
Comparison of Literature Abundance Determinations for NGC 40

Work	He/H	O/H	N/H	S/H	C/H
Perinotto	4.73e-2	7.24e-4	8.86e-5	2.80e-6	...
Liu	1.2e-1	4.9e-4	8.5e-5	2.6e-6	6.9e-4
Clegg	>0.044	8.4e-4	2.4e-4	3.9e-6	1.0e-3
Pottasch	>0.046	5.3e-4	1.3e-4	5.6e-6	1.9e-3
LGMR10	1.2e-1	4.1e-5	...	...	...
This work	0.9e-1	1.9e-4	6.8e-5	6.8e-6	6.5e-4

We have also included dust in our model, even though we have not explored the added parameter space to fully constrain the possibilities. However, with the assumption that the dust is mixed with the gas and adopting a dust-to-gas ratio by mass of 0.0015 as well as a typical MRN composition, we were able to reproduce the main characteristics of the observed infrared features as can be seen in Figure 6. A discrepancy is seen in the interval of 10–20 μm with the continuum showing lower values than observed. The difference could be due to a denser inner region (and thus hotter) such as a disk, which we have not included.

In Table 3, we compare the abundances form other works to the values obtained from our model fit. The first thing to note is the lack of agreement between empirical literature determinations as well as reliable confidence intervals. This is somewhat troubling since all the empirical methods are quite similar. The major differences are which portion of the nebula was considered and which ionization correction factor was used, indicating that much more work needs to be done in these areas if a reliable empirical method is to be developed. Even so we can say that the results are roughly correct in terms of order of magnitude. It is important to note, however, that our method does not rely on artificial correction factors such as filling factors or ionization correction factors, leading to results less dependent on assumptions.

With all the considerations above we believe that our model nicely ties in many pieces of the NGC 40 puzzle. However, much still needs to be done to definitely eliminate discrepancies, especially in abundance determinations as well defining the evolutionary state of these objects, and the good agreement of many different facets of the modeling process as done in this work suggests a possible way to pursue this.

H. Monteiro thanks CNPq for the financial support (no. 470135/2010-7) and D.F.G. thanks the financial support of the Brazilian agency FAPESP (no. 2009/10102-0).

REFERENCES

Acker, A., Ochsenbein, F., Stenholm, B., Tylenda, R., Marcout, J., & Schohn, C. 1994, Strabourg-ESO Catalogue of Galactic Planetary Nebulae (Garching: ESO)
Akashi, M., & Soker, N. 2008, MNRAS, 391, 1063
Baessgen, M., Diesch, C., & Grewing, M. 1990, A&A, 237, 201
Balick, B. 1987, AJ, 94, 671
Balick, B., Gonzalez, G., Frank, A., & Jacoby, G. 1992, ApJ, 392, 582
Blöcker, T. 1995, A&A, 299, 755
Carrasco, L., Serrano, A., & Costero, R. 1983, RevMexAA, 8, 187
Chu, Y.-H., Jacoby, G. H., & Arendt, R. 1987, ApJS, 64, 529
Clegg, R. E. S., Seaton, M. J., Peimbert, M., & Torres-Peimbert, S. 1983, MNRAS, 205, 417
Cohen, M., Barlow, M. J., Liu, X.-W., & Jones, A. F. 2002, MNRAS, 332, 879
Ercolano, B., Barlow, M. J., & Storey, P. J. 2005, MNRAS, 362, 1038
Ercolano, B., Barlow, M. J., Storey, P. J., & Liu, X.-W. 2003, MNRAS, 340, 1136
Falceta-Gonçalves, D., Abraham, Z., & Jatenco-Pereira, V. 2006, MNRAS, 371, 1295
Falceta-Gonçalves, D., Caproni, A., Abraham, Z., de Gouveia Dal Pino, E. M., & Duarte, D. M. 2010a, ApJ, 713, L74
Falceta-Gonçalves, D., de Gouveia Dal Pino, E. M., Gallagher, J. S., & Lazarian, A. 2010b, ApJ, 708, L57
Falceta-Gonçalves, D., Lazarian, A., & Houde, M. 2010c, ApJ, 713, 1376
Frank, A., Balick, B., & Livio, M. 1996, ApJ, 471, L53
García-Segura, G. 1997, ApJ, 489, L189
García-Segura, G., Langer, N., Różyczka, M., & Franco, J. 1999, ApJ, 517, 767
García-Segura, G., López, J. A., & Franco, J. 2005, ApJ, 618, 919
Henney, W. J., Arthur, J. S., Williams, R. J. R., & Ferland, G. J. 2005, ApJ, 621, 328
Hony, S., Waters, L. B. F. M., & Tielens, A. G. G. M. 2001, A&A, 378, L41
Icke, V., Balick, B., & Frank, A. 1992, A&A, 253, 224
Icke, V., Preston, H. L., & Balick, B. 1989, AJ, 97, 462
Koesterke, L., Dreizler, S., & Rauch, T. 1998, A&A, 330, 1041
Kwok, S. 2008, in IAU Symp. 252, The Art of Modeling Stars in the 21st Century, ed. L. Deng & K. L. Chan (Cambridge: Cambridge Univ. Press), 197
Leal-Ferreira, M. L., Gonçalves, D. R., Monteiro, H., & Richards, J. W. 2011, MNRAS, 411, 1395 (LGMR10)
Lee, C.-F., Hsu, M.-C., & Sahai, R. 2009, ApJ, 696, 1630
Lee, C.-F., & Sahai, R. 2003, ApJ, 586, 319
Lee, C.-F., & Sahai, R. 2004, ApJ, 606, 483
Liu, Y., Liu, X.-W., Luo, S.-G., & Barlow, M. J. 2004, MNRAS, 353, 1231 (LLLB04)
Londrillo, P., & Del Zanna, L. 2000, ApJ, 530, 508
Martin, J., Xilouris, K., & Soker, N. 2002, A&A, 391, 689
Mathis, J. S., Rumpl, W., & Nordsieck, K. H. 1977, ApJ, 217, 425
Meaburn, J., Lopez, J. A., Bryce, M., & Mellema, G. 1996, A&A, 307, 579
Monteiro, H., Morisset, C., Gruenwald, R., & Viegas, S. M. 2000, ApJ, 537, 853
Monteiro, H., Schwarz, H. E., Gruenwald, R., Guenthner, K., & Heathcote, S. R. 2005, ApJ, 620, 321
Monteiro, H., Schwarz, H. E., Gruenwald, R., & Heathcote, S. R. 2004, ApJ, 609, 194
Montez, R., Jr., Kastner, J. H., De Marco, O., & Soker, N. 2005, ApJ, 635, 381
Morisset, C., & Georgiev, L. 2009, A&A, 507, 1517
Phillips, J. P., & Marquez-Lugo, R. A. 2011, RevMexAA, 47, 83
Pottasch, S. R., & Bernard-Salas, J. 2010, A&A, 517, A95
Sabbadin, F., Cappellaro, E., Benetti, S., Turatto, M., & Zanin, C. 2000, A&A, 355, 688
Sahai, R., & Trauger, J. T. 1998, AJ, 116, 1357
Schwarz, H. E., & Monteiro, H. 2006, ApJ, 648, 430
Stanghellini, L., Corradi, R. L. M., & Schwarz, H. E. 1993, A&A, 279, 521
Stanghellini, L., Villaver, E., Manchado, A., & Guerrero, M. A. 2002, ApJ, 576, 285
Stasińska, G., & Szczerba, R. 1999, A&A, 352, 297
Vassiliadis, E., & Wood, P. R. 1994, ApJS, 92, 125
Werner, K., & Herwig, F. 2006, PASP, 118, 183
Williams, R. J. R. 2002, MNRAS, 331, 693